

pubs.acs.org/acsaelm Article

# Determination of the $\beta$ to $\gamma$ Phase Transformation Mechanism in Scand Al-Alloyed $\beta$ -Ga<sub>2</sub>O<sub>3</sub> Crystals

Andrew R. Balog,\* Channyung Lee, Daniel Duarte-Ruiz, Sai Venkata Gayathri Ayyagari, Jani Jesenovec, Adrian E. Chmielewski, Leixin Miao, Benjamin L. Dutton, John McCloy, Caterina Cocchi, Elif Ertekin, and Nasim Alem\*



Cite This: https://doi.org/10.1021/acsaelm.4c00762



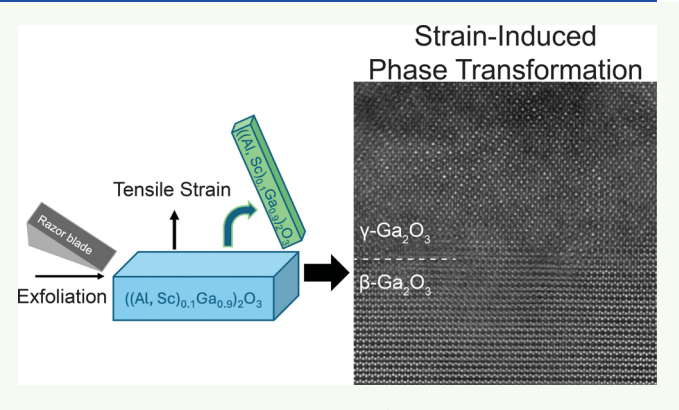
**ACCESS** 

Metrics & More

Article Recommendations

Supporting Information

**ABSTRACT:** β-Ga<sub>2</sub>O<sub>3</sub> is a promising ultrawide bandgap semiconductor for next-generation power electronics, but the unintended formation of γ-Ga<sub>2</sub>O<sub>3</sub> in β-Ga<sub>2</sub>O<sub>3</sub> crystals has been observed in a variety of situations. Such defective inclusions, resulting from growth kinetics or ion-induced damage, can degrade the material performance and alter the local electronic structure. Previous studies have only examined the presence of γ-Ga<sub>2</sub>O<sub>3</sub> in β-Ga<sub>2</sub>O<sub>3</sub> thin-film structures. In this work, we observe the ubiquitous formation of a thin γ-Ga<sub>2</sub>O<sub>3</sub> layer on the surface of mechanically exfoliated melt grown Al- and Sc-alloyed β-Ga<sub>2</sub>O<sub>3</sub> single crystals and characterize the atomic scale structure across the interface using scanning transmission electron microscopy. Direct imaging paired with electron diffraction confirms γ-Ga<sub>2</sub>O<sub>3</sub> formation, and



orientation relationships are determined across the interface. Electron energy loss spectroscopy identifies the O K-edge spectral fingerprint of  $\gamma$ -Ga<sub>2</sub>O<sub>3</sub>, while many-body perturbation theory on top of density functional theory explains the shift of the spectral intensity between  $\beta$ - and  $\gamma$ -Ga<sub>2</sub>O<sub>3</sub> as an interplay of excitonic and electronic effects. Further first-principles studies evaluate the role of strain on phase stability and identify that at an 8.5% tensile strain,  $\gamma$ -Ga<sub>2</sub>O<sub>3</sub> becomes energetically favored over  $\beta$ -Ga<sub>2</sub>O<sub>3</sub>. Stabilization of the  $\beta$  phase of Ga<sub>2</sub>O<sub>3</sub> under compressive stress is further confirmed through electron diffraction studies of the regions surrounding Vickers indentations. Phase stability is also observed to be independent of the alloying element. These findings confirm the capability for  $\gamma$ -Ga<sub>2</sub>O<sub>3</sub> to occur under extreme environments while also providing evidence that strain is the underlying driving force causing the phase transformation.

**KEYWORDS:** gallium oxide, transmission electron microscopy, electron energy loss spectroscopy, wide-band gap semiconductors, defects, phase transformation

# INTRODUCTION

 $\beta$ -Ga<sub>2</sub>O<sub>3</sub> is an emerging material of extreme interest for nextgeneration power semiconductors due to its ultrawide band gap of 4.8 eV, critical breakdown field of 8 MV/cm, and proliferation of high quality melt grown crystals and substrates. 1-5 Ga<sub>2</sub>O<sub>3</sub> is known to exist in six different polymorphs, including the monoclinic beta  $(\beta)$  phase (space group C2/m), being the most stable, and the less understood defective cubic spinel gamma ( $\gamma$ ) phase (space group Fd $\overline{3}$ m), being the least stable.<sup>6</sup> Much effort has been taken to study and characterize defects in  $\beta$ -Ga<sub>2</sub>O<sub>3</sub>, especially at the atomic scale, as such knowledge is key for controlling properties and accommodating dopants. 7-12 Prior studies have considered a wide range of dopants and alloys while also examining many different device structures and interface types. 13-17 Interestingly, recent studies in the literature have shown the propensity for  $\gamma$ -Ga<sub>2</sub>O<sub>3</sub> to appear as a defective inclusion in  $\beta$ -Ga<sub>2</sub>O<sub>3</sub>, especially at the surface of doped and aluminum-alloyed thin

films. <sup>14,16,18,19</sup> Understanding the structure of  $\gamma$ -Ga<sub>2</sub>O<sub>3</sub> and the conditions under which it forms in  $\beta$ -Ga<sub>2</sub>O<sub>3</sub> is vital to refining growth and processing techniques as well as ensuring device stability, operation, and performance.

While  $\gamma$ -Ga<sub>2</sub>O<sub>3</sub> has been observed in alloyed thin films, alloying Ga<sub>2</sub>O<sub>3</sub> has been primarily studied as a way of tuning the material's band gap. Alloying with Al and Sc has been demonstrated to increase the band gap of  $\beta$ -Ga<sub>2</sub>O<sub>3</sub>, opening new possibilities in device application and design due to its tunable gap.<sup>20,21</sup> However, the lowest energy polymorphs of

Received: April 26, 2024
Revised: September 10, 2024
Accepted: September 11, 2024



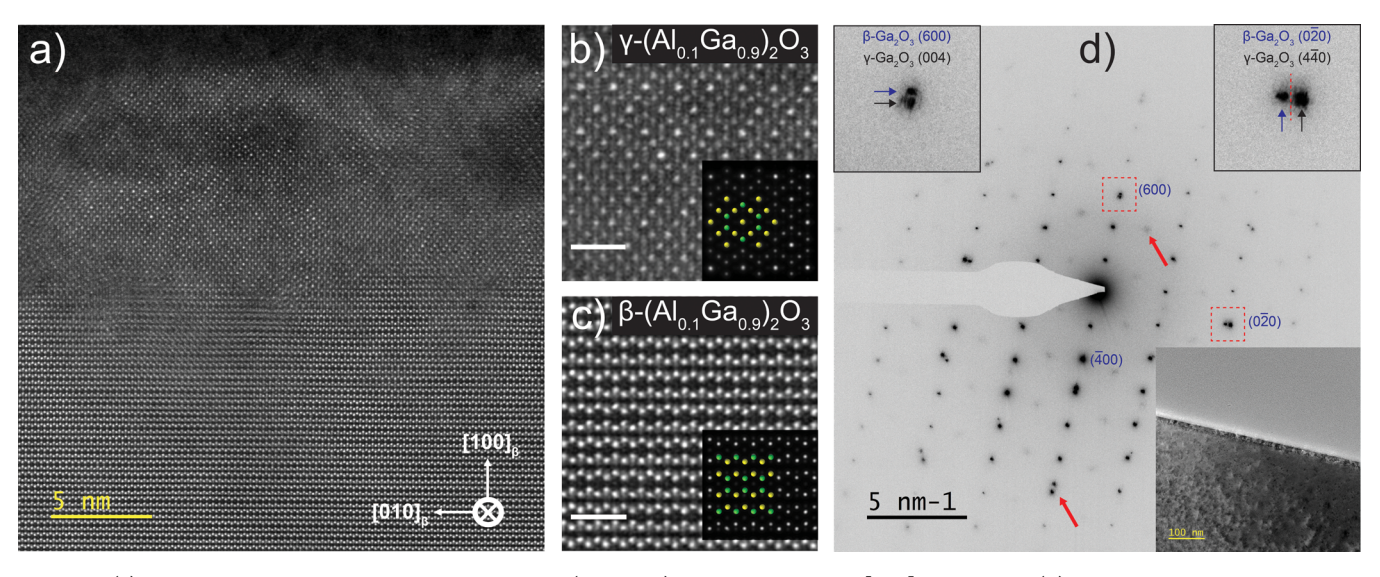


Figure 1. (a) ADF-STEM image of the  $\gamma/\beta$  interface in a  $\beta$ -(Al $_{0.1}$ Ga $_{0.9}$ ) $_2$ O $_3$  crystal from the  $[001]_{\beta}$  projection. (b) Magnified inset of the  $\gamma$  region, showing structural match with the [110]  $\gamma$ -Ga $_2$ O $_3$  projection. Tetrahedrally coordinated gallium atoms are shown in green, while octahedrally coordinated gallium atoms are shown in yellow. (c) Magnified inset of the  $\beta$  region with a [001] structural overlay. STEM image simulations are included to demonstrate the agreement between simulated images of the structures and the experimental STEM image. Scale bars in both (b,c) are 1 nm. (d) Electron diffraction pattern taken from a surface region of the crystal. Faint reflections from the  $\gamma$ -Ga $_2$ O $_3$  layer are visible, as well as separate reflections splitting at higher order planes, both of which are denoted by red arrows. Insets within the pattern better show the splitting of diffraction reflections at specified positions in the reciprocal space.

 $Al_2O_3$  and  $Sc_2O_3$  also possess crystal structures different from  $\beta$ - $Ga_2O_3$ , with  $Al_2O_3$  preferring rhombohedral corundum and  $Sc_2O_3$  preferring cubic bixbyite. 22,23 Resulting differences in ionic radii and bond length may contribute to structural instability and strain and could also induce the formation of defects and phase transformations away from the preferred monoclinic phase of  $Ga_2O_3$ . Thus, characterization of the crystal structure and defects within the alloyed systems is necessary to enable device development and understanding phase stability within  $Ga_2O_3$ .

While prior studies have shown that the various  $Ga_2O_3$  polymorphs can easily be formed under various growth and annealing conditions due to their small energy differences, recent work by Huang et al. has also theorized that an accumulation of strain can trigger the  $\beta$  to  $\gamma$  phase transformation. However, this theory and prior studies on  $\gamma$ -Ga $_2O_3$  have focused on its formation and presence in thin films, since melt grown  $\beta$ -Ga $_2O_3$  single crystals have not yet shown evidence of  $\gamma$ -Ga $_2O_3$  presence. Have  $\frac{1}{4}$ , 16, 18, 19

In this study, we present the ubiquitous formation of  $\gamma$ - $Ga_2O_3$  on the surface of alloyed (100)  $\beta$ - $Ga_2O_3$  crystals grown via the Czochralski method after mechanical cleavage regardless of the alloying composition. Atomic resolution scanning transmission electron microscopy (STEM) and advanced spectroscopy are used to identify the structure of γ-Ga<sub>2</sub>O<sub>3</sub> as well as its local chemical and electronic environment. Here, theoretical studies are combined with experimental imaging and spectroscopy to provide insight into the chemical structure of the two phases and to predict excitonic and electronic shifts between them. We also perform simulations to confirm that under certain strain conditions, the  $\gamma$  phase becomes energetically favored over the  $\beta$  phase, indicating that particular strain conditions experienced at the surface during cleavage may promote a buildup of strain and therefore the formation of  $\gamma$ -Ga<sub>2</sub>O<sub>3</sub>. Such stress conditions may be responsible for promoting the  $\beta$  to  $\gamma$  phase transformation internally within bulk  $\beta$ -Ga<sub>2</sub>O<sub>3</sub>

# ■ RESULTS AND DISCUSSION

Figure 1a shows an annular dark field-STEM (ADF-STEM) image of an unexpected, secondary phase layer observed on the surface of a crystal alloyed with aluminum in a nominal composition of  $\beta$ -(Al<sub>0.1</sub>Ga<sub>0.9</sub>)<sub>2</sub>O<sub>3</sub>. ADF-STEM allows for accurate imaging of the atomic structure due to its sensitivity to the atomic number of the constituent atoms.<sup>26</sup> At first observation, this structure shows similarity to examples of [110]  $\gamma$ -Ga<sub>2</sub>O<sub>3</sub> observed in the literature. Regions of [110]  $\gamma$ - $Ga_2O_3$  are visible interspersed with overlapped layers of  $\gamma$ - $Ga_2O_3$ , matching the appearance of overlapped  $\gamma$ - $Ga_2O_3$  layers identified by prior literature. 16,19 This layer exhibits a depth of 10-20 nm across the entire surface of the sample. Figure 1b,c shows zoomed-in high-resolution ADF-STEM images of  $\gamma$ - $Ga_2O_3$  and  $\beta$ - $Ga_2O_3$  confirming the apparent presence of  $\gamma$ -Ga<sub>2</sub>O<sub>3</sub> on the surface of the crystal. STEM image simulations were conducted on models of both  $\gamma$ - and  $\beta$ -Ga<sub>2</sub>O<sub>3</sub> structures, shown via the insets in Figure 1b,c. These simulations demonstrate good agreement with the experimentally observed structures in STEM images. An increased concentration of Al interstitial atoms was also observed within several nanometers of the interface (Figure S1), while geometric phase analysis also showed the apparent formation of dislocations along the  $\gamma/\beta$  interface (Figure S1).<sup>27</sup> To further determine the interfacial structure, selected area electron diffraction (SAED) was performed with the SA aperture placed over the interface. Figure 1d shows the diffraction pattern taken from this sample, with the contrast inverted to better show new reflections from the secondary phase. Several rows of faint diffraction reflections are visible between the main rows of  $\beta$ -Ga<sub>2</sub>O<sub>3</sub> diffraction spots (indicated by a red arrow in Figure 1d), suggesting the development of an additional phase. Acquired from the [001] zone axis, the measurement of the reflections corresponding to the (600) and ( $\overline{020}$ ) planes in  $\beta$ - $Ga_2O_3$  shows reciprocal space vectors of 5.06 nm<sup>-1</sup> (0.198 nm) and 6.60 nm<sup>-1</sup> (0.152 nm), in good agreement with theoretical

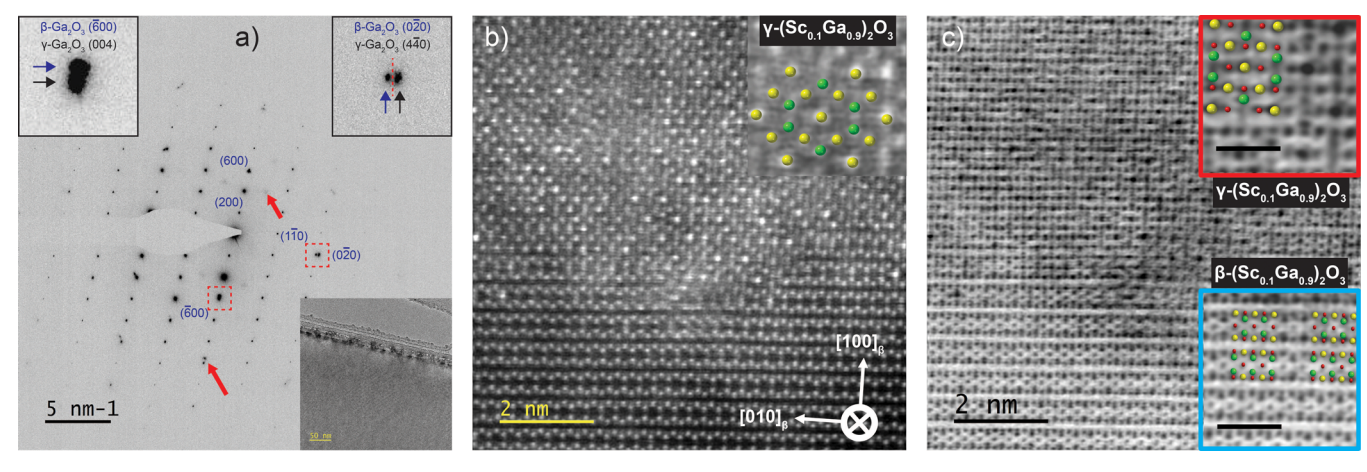


Figure 2. (a) SAED pattern from the surface region of a  $\beta$ -(Sc<sub>0.1</sub>Ga<sub>0.9</sub>)<sub>2</sub>O<sub>3</sub> crystal with contrast inverted to better show the development of additional and unexpected diffraction reflections, corresponding with those of γ-Ga<sub>2</sub>O<sub>3</sub>. (b) High resolution ADF-STEM image of the interfacial region from the  $[001]_{\beta}$  projection. Motif of [110] γ-Ga<sub>2</sub>O<sub>3</sub> is included to better show their structural match. Tetrahedrally coordinated gallium atoms are shown in green, while octahedrally coordinated gallium atoms are shown in yellow. (c) ABF-STEM image collected simultaneously with (b), revealing oxygen column positions represented by red circles. Again, a motif of the [110] γ-Ga<sub>2</sub>O<sub>3</sub> structure is overlaid, while a similar motif of [001] β-Ga<sub>2</sub>O<sub>3</sub> is overlaid in the bottom corner. Scale bars in the insets of (c) are 1 nm.

values for interplanar spacings in a [001]  $\beta$ -Ga<sub>2</sub>O<sub>3</sub> diffraction pattern.<sup>28-30</sup> The magnified insets in Figure 1d show these reflections starting to split at the  $(600)_{\beta}$  and  $(0\overline{2}0)_{\beta}$  lattice reflections, with blue arrows indicating the reflection matching  $\beta$ -Ga<sub>2</sub>O<sub>3</sub>. The black arrows indicate the extra reflections splitting off, measured at 4.86 nm<sup>-1</sup> (0.206 nm) and 6.69 nm<sup>-1</sup> (0.149 nm), respectively, corresponding to the (004) and (440) families of planes in  $\gamma$ -Ga<sub>2</sub>O<sub>3</sub>.<sup>31</sup> Faint diffraction spots can also be seen between the (200) and (110)  $\beta$ -Ga<sub>2</sub>O<sub>3</sub> reflections (indicated by the red arrows) that do not belong to the  $\beta$ -phase from the [001] zone axis. Measuring a reciprocal space distance of 3.98 nm<sup>-1</sup>, these spots correspond to the (113) family of planes in  $\gamma$ -Ga<sub>2</sub>O<sub>3</sub>. Through the electron diffraction studies coupled with high-resolution STEM imaging and simulation, we conclusively identify the  $\gamma$  phase of Ga<sub>2</sub>O<sub>3</sub>. Additionally, orientation relationships of  $(600)_{\beta} \parallel (004)_{\gamma}$  and  $(0\overline{2}0)_{\beta} \parallel (4\overline{4}0)_{\gamma}$  can be distinguished between the two phases from the diffraction pattern. Prior studies have observed the presumed diffraction pattern of [110] γ-Ga<sub>2</sub>O<sub>3</sub> in an ioninduced transformation layer, and the faint intensity visible here matches well with that previously reported γ-Ga<sub>2</sub>O<sub>3</sub> diffraction pattern. 32

Similar experiments were performed on crystals having a nominal composition of  $\beta$ -(Sc<sub>0.1</sub>Ga<sub>0.9</sub>)<sub>2</sub>O<sub>3</sub>. Figure 2a shows a SAED pattern from a [001]  $\beta$ -(Sc<sub>0.1</sub>Ga<sub>0.9</sub>)<sub>2</sub>O<sub>3</sub> crystal, revealing the structure of the film with a thin layer of the  $\gamma$  phase on top of it. Again, a faint intensity is visible between the main  $\beta$ -Ga<sub>2</sub>O<sub>3</sub> reflections, which can be assigned to the (113) planes of γ-Ga<sub>2</sub>O<sub>3</sub>. Reflection splitting similar to that discussed in Figure 1d is also observed here, and similar orientation relationships are maintained across the interface, with  $(\overline{600})_{\beta}$  ||  $(00\overline{4})_{\nu}$  and  $(0\overline{2}0)_{\beta} \parallel (4\overline{4}0)_{\nu}$ . As in the  $\beta$ - $(Al_{0.1}Ga_{0.9})_2O_3$  sample, the depth of the apparent  $\gamma$  phase layer ranged from 10 to 20 nm across the entire sample lamella. A high-resolution transmission electron microscopy (HRTEM) image of the top region, with the γ-Ga<sub>2</sub>O<sub>3</sub> layer exhibiting a different contrast from the bulk  $\beta$ -Ga<sub>2</sub>O<sub>3</sub>, is shown in the Supporting Information (Figure S2). Fast Fourier transform (FFT) patterns taken from the indicated individual regions recover patterns closely resembling single phase  $\gamma$  or  $\beta$ -Ga<sub>2</sub>O<sub>3</sub>. The overall appearance of the FFT patterns for the entire image

closely matches that of the SAED patterns in Figures 1 and 2, further confirming the formation of an  $\gamma$ -Ga<sub>2</sub>O<sub>3</sub> layer on  $\beta$ -Ga<sub>2</sub>O<sub>3</sub>.

To further investigate and confirm the atomic structure of the  $\gamma$  phase in the  $\beta$ -(Sc<sub>0.1</sub>Ga<sub>0.9</sub>)<sub>2</sub>O<sub>3</sub> sample and the  $\gamma/\beta$ interfacial structure at the atomic scale, ADF and Annular Bright Field-STEM (ABF-STEM) imaging was performed, as shown in Figure 2b,c. These display complementary ADF and ABF-STEM images from a region of the  $\gamma/\beta$  interface. ABF-STEM is crucial for identifying crystal structure due to its ability to image lighter elements and structural distortions, in this case oxygen column positions.<sup>33</sup> The use of ABF-STEM is further necessary due to the projection of slightly overlapped  $\beta$ -Ga<sub>2</sub>O<sub>3</sub> layers resembling the projection of [110]  $\gamma$ -Ga<sub>2</sub>O<sub>3</sub> in ADF-STEM imaging, as described by Chang et al. 19 Considering that the  $\beta$ -Ga<sub>2</sub>O<sub>3</sub> Al- and Sc-alloyed crystals were mechanically cleaved, with some stress applied to the surface, it was possible for a stress condition to create the overlapped  $\beta$ -Ga<sub>2</sub>O<sub>3</sub> projection and not  $\gamma$ -Ga<sub>2</sub>O<sub>3</sub>.

In order to discern between the two scenarios, direct imaging of the oxygen sublattice is necessary, as enabled by ABF-STEM. The inset of Figure 2b shows how the observed pattern of Ga atoms in this sample also matches the [110] projection of  $\gamma$ -Ga<sub>2</sub>O<sub>3</sub>, with the green and yellow circles representing tetrahedrally and octahedrally coordinated Ga, respectively. Regions of unambiguous [110] γ-Ga<sub>2</sub>O<sub>3</sub> were identified, as well as other regions showing the overlapped motifs observed in Figure 1. It is also important to note the structure of the  $\gamma/\beta$  interface. The  $\gamma$ -Ga<sub>2</sub>O<sub>3</sub> layer appears smooth on the micron scale covering the  $\beta$  phase (Figure S3), but the interface exhibits step edges and jumps on the atomic scale as seen in Figure 2b. The bright-field TEM (BF-TEM) image shown in Figure S3 further demonstrates how the two phases appear with different contrast, indicative of a phase transformation and the presence of  $\gamma$ -Ga<sub>2</sub>O<sub>3</sub> in the Sc-alloyed sample. The disorder present in the interfacial structure lends weight to the argument of Huang et al., that a buildup of strain and defects triggers a relaxation into the  $\gamma$  phase.<sup>24,25</sup> Yoo et al. also theorized that the surface energy of γ-Ga<sub>2</sub>O<sub>3</sub> may play a role in its formation at the crystal surface, but corresponding computational studies of the  $\gamma/\beta$  surface energy relationship

**ACS Applied Electronic Materials** 

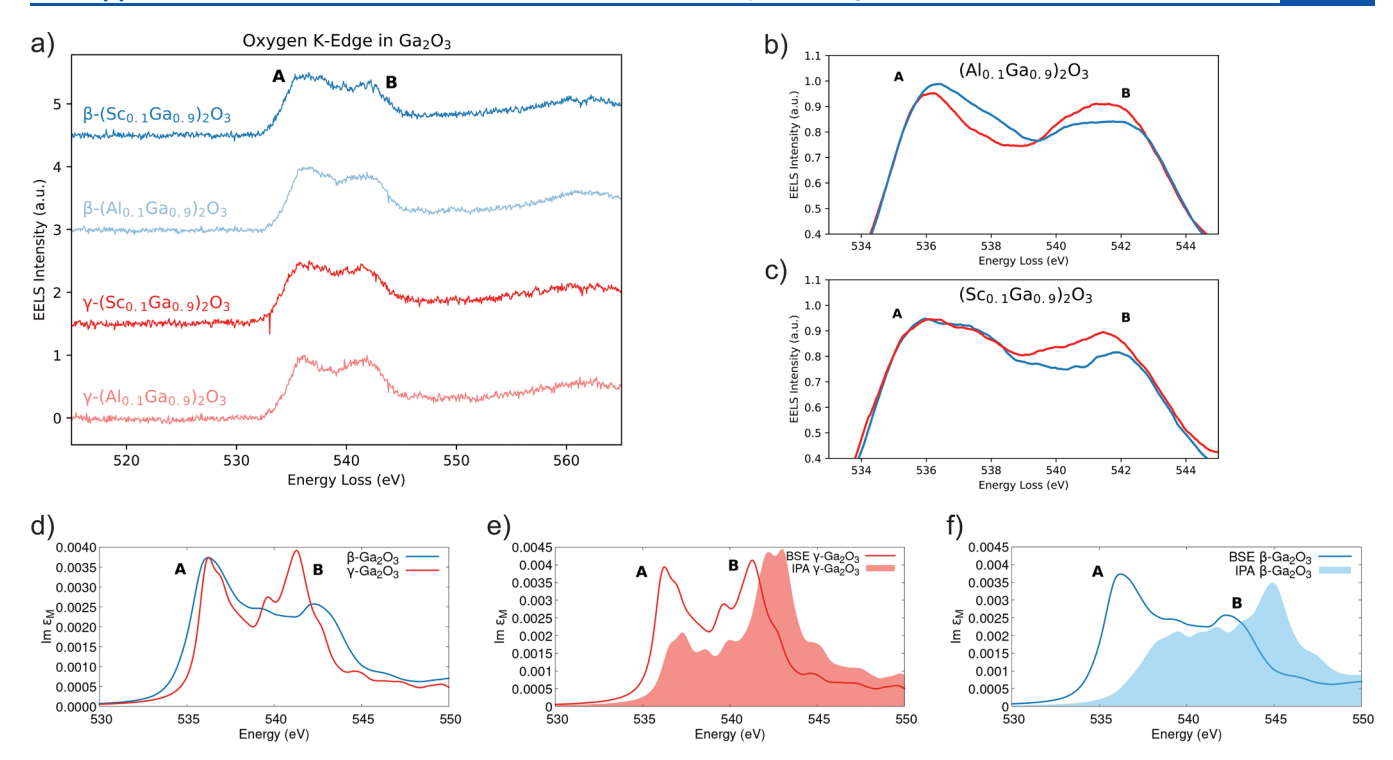


Figure 3. (a) O K-edge spectra of (from top to bottom):  $\beta$ -(Sc<sub>0.1</sub>Ga<sub>0.9</sub>)<sub>2</sub>O<sub>3</sub> (dark blue),  $\beta$ -(Al<sub>0.1</sub>Ga<sub>0.9</sub>)<sub>2</sub>O<sub>3</sub> (light blue),  $\gamma$ -(Sc<sub>0.1</sub>Ga<sub>0.9</sub>)<sub>2</sub>O<sub>3</sub> (dark red), and  $\gamma$ -(Al<sub>0.1</sub>Ga<sub>0.9</sub>)<sub>2</sub>O<sub>3</sub> (light red). (b) Magnified view of the double peak structure in a (Al<sub>0.1</sub>Ga<sub>0.9</sub>)<sub>2</sub>O<sub>3</sub> sample, showing the A:B ratio increasing for  $\gamma$ -(Al<sub>0.1</sub>Ga<sub>0.9</sub>)<sub>2</sub>O<sub>3</sub>. (c) Magnified view of the double peak structure in a (Sc<sub>0.1</sub>Ga<sub>0.9</sub>)<sub>2</sub>O<sub>3</sub> sample, showing the A:B ratio increasing for  $\gamma$ -(Sc<sub>0.1</sub>Ga<sub>0.9</sub>)<sub>2</sub>O<sub>3</sub>. (d) O K-edge spectra of  $\gamma$ - and  $\beta$ -Ga<sub>2</sub>O<sub>3</sub> calculated in their ideal structures by solving the Bethe–Salpeter equation (BSE) on top of DFT. O K-edge spectrum was computed from the solution of the BSE (solid line) and in the independent-particle approximation (IPA) of (e)  $\gamma$ -Ga<sub>2</sub>O<sub>3</sub> and (f)  $\beta$ -Ga<sub>2</sub>O<sub>3</sub>.

are still lacking. <sup>16</sup> X-ray energy dispersive spectroscopy (XEDS) studies did not demonstrate any significant segregation or compositional separation, indicating that stoichiometry was maintained during the phase transformation (Figure S4). The ABF-STEM image in Figure 2c shows a change in the oxygen sublattice from the  $\beta$  phase to the  $\gamma$  phase, with the inset structure again matching well with the [110]  $\gamma$ -Ga<sub>2</sub>O<sub>3</sub> projection. An overlay of the  $\beta$ -Ga<sub>2</sub>O<sub>3</sub> structure with oxygen positions is also shown in the bottom of Figure 2c for better comparison to the  $\gamma$ -Ga<sub>2</sub>O<sub>3</sub> oxygen sublattice. Thus, our HR-STEM and diffraction studies similarly uncover that mechanical exfoliation can lead to a  $\beta$ - to  $\gamma$ -phase transformation, with the interface indicating step edges and strain.

To further understand the local bonding and valence structure in each phase, monochromated electron energy loss spectroscopy (EELS) was performed on the samples. Cocchi et al. first examined the Electron-Loss Near Edge Structure (ELNES) of the oxygen K-edge in  $\beta$ -Ga<sub>2</sub>O<sub>3</sub> through a combination of computational simulation and TEM-EELS.34 Since then, the oxygen K-edge and ELNES fine structure of  $\beta$ - $Ga_2O_3$  have been well-studied and confirmed in the literature. The oxygen K-edge for the  $\beta$  phase is comprised of a double peak structure, with the first one (labeled "A") located at 536 eV, while the second peak, having less intensity, is around 540 eV (labeled "B" peak).<sup>34</sup> These represent excitations from 1s atomic orbitals to unoccupied plike states. Unfortunately, such an in-depth analysis is not yet available for the oxygen K-edge of γ-Ga<sub>2</sub>O<sub>3</sub>. An oxygen K-edge for γ-Ga<sub>2</sub>O<sub>3</sub> has also been published showing similar double peak features but does not discuss the interpretation of the edge structure and bonding.<sup>37</sup> Sharma et al. also performed X-

ray absorption spectroscopy (XAS) studies in undoped and Sm-doped samples of  $\gamma$ -Ga<sub>2</sub>O<sub>3</sub>, nanoparticles,<sup>38</sup> observing a double peak structure similar to our data.

Figure 3a shows spectra taken from oxygen K-edge EELS scans for the  $\beta$  and  $\gamma$  phases in both  $(Al_{0.1}Ga_{0.9})_2O_3$  and  $(Sc_{0.1}Ga_{0.9})_2O_3$  alloyed samples. These results for the  $\beta$ -phase collection regions of the two compositions match well with references in the literature, showing an A/B peak ratio of 1:0.9. Figure 3b,c shows in more detail the intensity of the B peak increasing in  $\gamma$ -Ga\_2O\_3 regardless of the alloy composition, much like the X-ray absorption Near Edge Structure (XANES) data reported by Sharma et al.  $^{38}$ 

Comparison of Gaussian deconvolutions for the double peak structure in the experimental EELS spectra for (Sc<sub>0.1</sub>Ga<sub>0.9</sub>)<sub>2</sub>O<sub>3</sub> (Figure S5) better illustrates a noticeable change in peak ratios from the  $\beta$  phase to the  $\gamma$  phase, demonstrating a clear difference in the bonding configuration between the two polymorphs. Scandium L-edge spectra were also collected for both the  $\gamma$  and  $\beta$  phase regions of  $(Sc_{0.1}Ga_{0.9})_2O_3$  (Figure S6).  $L_{2,3}$  edges of Sc are produced by excitations of  $2p_{1/2}$  and  $2p_{3/2}$ core electrons to unoccupied d-like states, thus approximating the unoccupied 3d density of states for the element. The L<sub>3a</sub> and L2a edges displayed a slight increase in their onset energy of 0.4 eV in the  $\gamma$  phase layer compared to  $\beta$ -(Sc<sub>0.1</sub>Ga<sub>0.9</sub>)<sub>2</sub>O<sub>3</sub>, with no other apparent differences in the edge fine structure fingerprint. Otherwise, the scandium L-edge spectra for both  $\beta$ - $(Sc_{0.1}Ga_{0.9})_2O_3$  and  $\gamma$ - $(Sc_{0.1}Ga_{0.9})_2O_3$  matches well with literature XANES fine structure values.<sup>39</sup> Here, the differences observed in the EELS spectra combined with the difference in structure identified via TEM and ADF-STEM provide a

**ACS Applied Electronic Materials** 

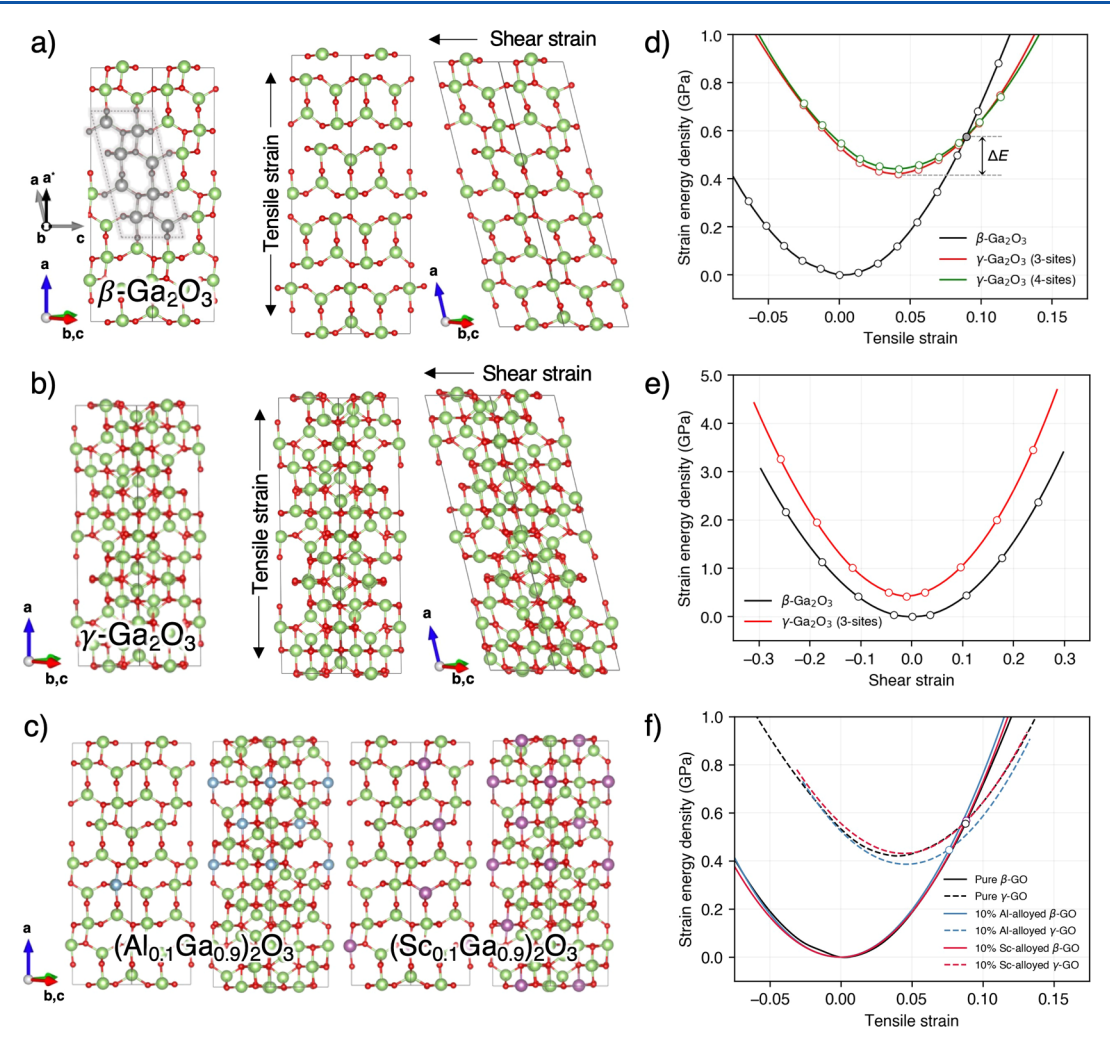


Figure 4. Atomic structures for (a)  $\beta$ -Ga<sub>2</sub>O<sub>3</sub> and (b)  $\gamma$ -Ga<sub>2</sub>O<sub>3</sub> showing the reference as well as applied tensile and shear strains, respectively, with the lowest energy 10% Al and Sc-alloyed structures shown in (c). Conventional unit cell of the β-phase is shown in (a) as a gray-colored image with respective conventional lattice vectors for comparison. (d) Relationship between the strain energy density and the applied uniaxial tensile strain along the a-axis (a\* axis in a conventional β-phase unit cell) under volume-fixed conditions. (e) Strain energy density vs applied shear strain along the a-bc direction (a\*c direction in a conventional β-phase unit cell) under volume-fixed conditions. Discrete circles indicate data points computed in DFT, while the solid lines represent a second-order polynomial fit. (f) Strain energy density of 10% Al and Sc-alloyed β- and γ-Ga<sub>2</sub>O<sub>3</sub> as a function of applied tensile strain along the a-axis under volume-fixed conditions. Intersection points are represented as the discrete circles.

thorough structural and spectroscopic understanding of the  $\gamma$ -Ga<sub>2</sub>O<sub>3</sub> polymorph.

To further investigate the spectral fingerprints of  $\beta$ - and  $\gamma$ -Ga<sub>2</sub>O<sub>3</sub> excited at the K-edge, computational studies using firstprinciples many-body theory were performed. This approach has been successfully employed to study core-level excitations in various gallium oxide polymorphs. 34,40 The results of this analysis, shown in Figure 3d, indicate that in both phases, the material exhibits a sharp peak at the onset, in agreement with the experiments. On the other hand, at higher energies, the intensity of the dominant resonance is different in the two phases. In the  $\beta$ -phase, the second peak in the O K-edge fine structure is remarkably weaker than the first one, as extensively discussed in previous work. <sup>17,34</sup> In the  $\gamma$ -phase, in contrast, the intensity of the second peak is slightly larger than the first one, and the two maxima are energetically closer than in the  $\beta$ phase. The comparison of the spectra computed by solving the Bethe-Salpeter equation (BSE) on top of density functional theory (DFT), with their counterpart obtained neglecting electron-hole correlations in the independent-particle approximation (IPA, Figure 3e,f), reveals a different role of excitonic

effects in the two polymorphs. While the first peak gains considerable intensity when the electron-hole interactions are accounted for in the BSE, confirming its excitonic nature in both phases, in the spectrum of  $\gamma$ -Ga<sub>2</sub>O<sub>3</sub> the second peak has a very similar broadening and intensity in both BSE and IPA results. This finding suggests that in γ-Ga<sub>2</sub>O<sub>3</sub>, this feature is less influenced by electron-hole Coulomb couplings. 41-44 On the other hand, in  $\beta$ -Ga<sub>2</sub>O<sub>3</sub>, the peaks visualized in Figure 3f bear an excitonic nature as extensively discussed previously by Cocchi et al.<sup>34</sup>: when electron-hole correlations are turned off (IPA), the main resonances in the spectrum differ from the BSE result in terms of oscillator strength distribution. We specify that the herein adopted term "exciton" is not limited to bound electron-hole pairs found inside the fundamental gap but extends to two-particle excitations in which Coulomb interactions modify their fingerprints compared to the independent-particle picture. A similar vocabulary was also used in previous work. 45-49 We also stress that the excitons analyzed here are characterized by holes in the core region. Note that BSE spectra are typically red-shifted compared to IPA spectra due to the inclusion of the attractive electron**ACS Applied Electronic Materials** 

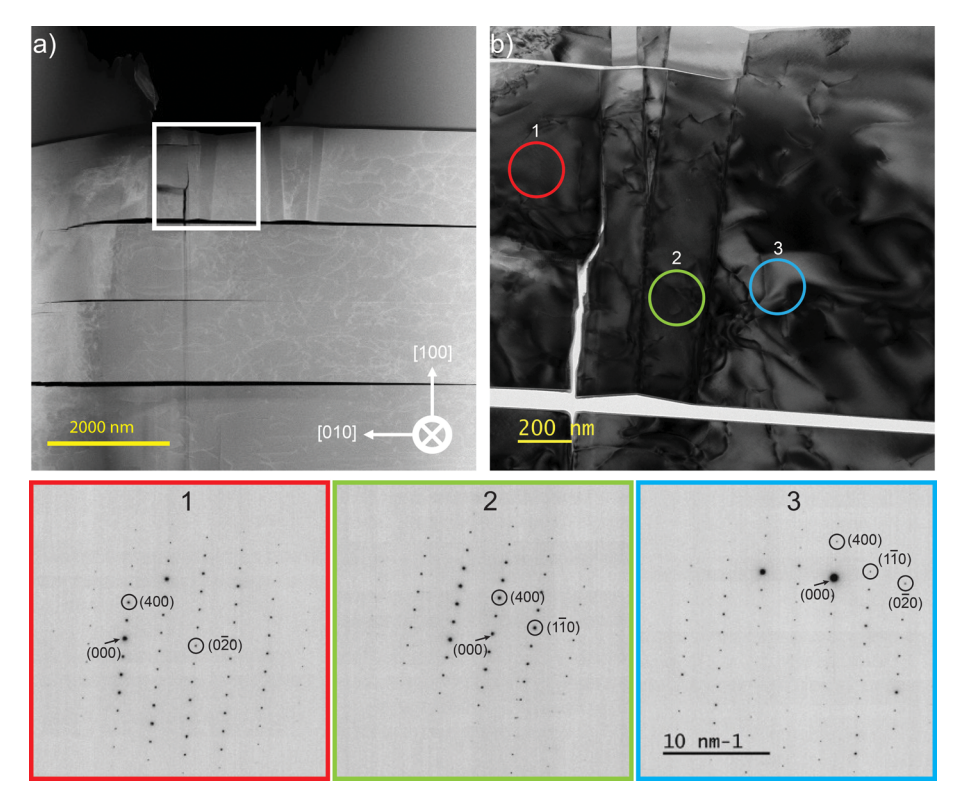


Figure 5. (a) ADF-STEM image of the 1 N Vickers indented sample after thinning to electron transparency. Depression caused by the indentation can be seen at the surface inclination on the left side of the sample. (b) BF-TEM image of the region around 1 N Vickers indentation normal to the (100) surface in a β-(Sc<sub>0.1</sub>Ga<sub>0.9</sub>)<sub>2</sub>O<sub>3</sub>. Intense dislocation, slip bands, and crack formation along the (100) cleavage plane is observed. Numbered and colored circles correspond to the location of the SA aperture used to collect the diffraction pattern displayed for each.

hole-screened Coulomb interaction. For further details about this formalism, we direct interested readers to specialized literature. 43,44,50

We hypothesize that the different weights of excitonic effects observed in the BSE spectra of  $\beta$ - and  $\gamma$ -Ga<sub>2</sub>O<sub>3</sub> are related to the different dielectric screening characterizing the two different polymorphs, with the  $\gamma$ -phase exhibiting a larger screening than the  $\beta$ -phase (Figure S7). While this result may be partially affected by the metallic character of  $\gamma$ -Ga<sub>2</sub>O<sub>3</sub> obtained using a defective spinel structure with vacancies of  $\gamma$  leading to the n-type doping, the agreement with the trends obtained from experiments supports our speculation. This may not be the exclusive reason for the observed spectral behavior of the two Ga<sub>2</sub>O<sub>3</sub> polymorphs, but the complexity of the material, especially in the  $\gamma$ -phase, prevents us from further extending this theoretical analysis. It is worth noting that alloying  $\gamma$ -Ga<sub>2</sub>O<sub>3</sub> with Al or Sc increases the band gap with the resulting crystal being semiconducting (Figure S8).

The addition of 10 mol % of Al or Sc does not show any clear impacts to the experimental oxygen K-edge of the two alloys compared to unalloyed  $\beta$ -Ga<sub>2</sub>O<sub>3</sub>. While our imaging, diffraction, and spectroscopy studies all indicate the presence of the  $\gamma$  phase as a thin film over the  $\beta$  phase of Ga<sub>2</sub>O<sub>3</sub>, the alloying elements, Sc and Al, may not have a specific role in the phase transformation, as the gamma phase was observed in both systems. However, the samples were prepared through exfoliation of pieces from the boule after growth via mechanical exfoliation and cleaving the crystal with a surface normal to the [100] direction. This also means that the crystals used for TEM lamellae fabrication did not come from the exterior surface of the boule and instead represent interior surfaces of the boule. Therefore, the cause of this  $\beta$  to  $\gamma$ 

transformation occurs between the growth and TEM lamella preparation steps. Extreme care was taken to protect the surface of the crystals from ion contamination during sample preparation via the use of a protective carbon layer before the fabrication step. Considering these preventative steps,  $\gamma$ -Ga<sub>2</sub>O<sub>3</sub> was still observed across multiple source crystals and TEM samples that were prepared through the exfoliation process, which led us to believe that the cause of the phase transformation likely lies in the exfoliation step.

Considering that the  $\gamma$ -phase samples were observed following exfoliation, local stress near the top layer undergoing exfoliation may lead to a phase transformation. Metastable polymorphs far from equilibrium in both  $Ga_2O_3$  and other oxides are known to become stabilized at the surface under various mechanical strains, such as epitaxial strains imposed by the substrate during thin-film growth and high tensile strains during fracture or exfoliation. To investigate the underlying mechanism of the formation of a metastable  $\gamma$ -phase during exfoliation, we conducted a series of first-principles simulations using DFT to determine relative phase energies as a function of mechanical strain considering both uniaxial tensile and shear strain (Figure 4).

While Figure 4a—c represents models of unalloyed and alloyed  $\beta$ - and  $\gamma$ -Ga<sub>2</sub>O<sub>3</sub> under tensile and shear strain, Figure 4d illustrates the variation of strain energy density as a function of uniaxial strain along the *a*-axis ( $a^*$  direction in the conventional  $\beta$ -phase unit cell) under volume-fixed conditions (i.e., lateral shrinkage (expansion) was imposed as tensile (compressive) strain was applied). Since the  $\gamma$  phase forms as a defect spinel structure, we used both 3-site and 4-site models to describe the distribution of atoms in the disordered phase, both of which have been shown to accurately describe most

physical properties. 53 For the  $\gamma$  phase, both models show larger lattice constants of 25.01 and 25.02 Å, respectively, compared to the  $\beta$  phase lattice constant of 24.02 Å, suggesting that large tensile strains may stabilize the  $\gamma$  phase. For the fully relaxed  $\beta$ and  $\gamma$  phase, the energy difference is 28.38 meV/atom, with the 3-site model being slightly more stable than, but similar to, the 4-site model consistent with Ratcliff et al.<sup>53</sup> As indicated by the crossing points of the energy curves (the gray circle), the  $\gamma$ phase becomes stable relative to the  $\beta$  phase at a critical tensile strain of around 0.085 (Å/Å). Additionally, while the shape of the strain energy density curves suggests that the phase transformation is induced by elongational tensile strain, compressive strain does not result in transformation as shown on the left-hand side of Figure 4d. For further evidence that compression does not lead to phase transformation, a  $\beta$ -(Sc<sub>0.1</sub>Ga<sub>0.9</sub>)<sub>2</sub>O<sub>3</sub> crystal was deformed by using a load of 1 N through the Vickers indentation technique. Initial electron diffraction studies of the locally deformed indented region with identical compositions and surface orientations to those considered in the first part of this study were collected. Figure 5a shows a low-magnification STEM image taken of the deformation region around the indentation. Concentrated dislocation formation, cracks along the (100) cleavage plane, and grain formation were observed. These defects are better visualized in Figure 5b, an BF-TEM image of the white boxed region of Figure 5a. Several diffraction patterns were collected from this area (color coded patterns 1, 2, and 3). None displayed evidence of γ-Ga<sub>2</sub>O<sub>3</sub> formation, instead pointing toward the formation of low angle grain boundaries with inplane rotations of  $\sim 8.5^{\circ}$  between them. This further supports DFT predictions that compression favors the stabilization of  $\beta$ -Ga<sub>2</sub>O<sub>3</sub>. Further STEM investigation of biased Au/Ni/β-Ga<sub>2</sub>O<sub>3</sub> Schottky Barrier Diodes also revealed the presence of γ-Ga<sub>2</sub>O<sub>3</sub> in delaminated regions along the Ni/β-Ga<sub>2</sub>O<sub>3</sub> interface surrounded by vacuum (Figure S9).<sup>54</sup> This further indicates that other types of external stress, such as thermal stimuli and electric fields, can favor formation of the metastable γ-Ga<sub>2</sub>O<sub>3</sub>.

To better understand how the introduction of tensile strain favors the formation of the  $\gamma$  phase, we consider the atomic structures of  $\beta$ - and  $\gamma$ -Ga<sub>2</sub>O<sub>3</sub> at the critical strain in Figure 4a,b. These structures show that more Ga–O bonds along the a-axis are possible in the presence of randomly displaced Ga cations in the disordered  $\gamma$  phase. Compared to the ordered cation structure of the  $\beta$  phase, which occasionally lacks vertical bonds along the a-axis, the additional bond formation is likely to favor disorder and formation of  $\gamma$ . The elongation of the lattice under tensile strain is hypothesized to facilitate a structural reconfiguration that weakens Ga–O bonds and creates facile reaction pathways for the sequential splitting of tetragonal Ga atoms to form  $(V_{Ga(I)}-Ga_i)_n$  chains crucial for the  $\gamma$ -phase transition.

Figure 4e shows how the  $\gamma$  and  $\beta$  phase energies vary as a function of applied shear strain, also considered here for completeness. We define the  $x_1$ ,  $x_2$ , and  $x_3$  axes as the three orthogonal principal axes referenced to the conventional  $\beta$  phase crystal structure as follows: the  $x_2$  and  $x_3$  axes are along the b and c crystallographic directions, respectively, and the  $x_1$  axis is perpendicular to the  $x_2-x_3$  plane. The  $x_1$  axis is parallel to not the a axis but the  $a^*$  axis. We applied shear strain in the  $x_1-x_3$  plane. We observed no crossing points between the strain energy curves here, even under extremely high shear strains, suggesting that the shear strain is not associated with the observed formation of the  $\gamma$  phase. It is also important to

note that these simulations represent idealized conditions of strain with the applied exfoliation potentially generating a complex strain state comprising a mix of those considered. Alloying with other isovalent oxides, such as Sc<sub>2</sub>O<sub>3</sub> and Al<sub>2</sub>O<sub>3</sub>, which prefer crystal structures different from the monoclinic  $\beta$ -Ga<sub>2</sub>O<sub>3</sub>, can introduce additional structural disorder by causing bond distortions due to mismatch in preferred bonding coordinates and variations in ionic radii. This disorder could contribute to the phase instability of beta-phase structures and facilitate the formation of defects, such as interstitials, vacancies, and extended defect complexes, thereby potentially promoting phase transformation by reducing both the reaction coordinates and the energy barrier. 14,17,55 To understand the role of alloying with Sc<sub>2</sub>O<sub>3</sub> and Al<sub>2</sub>O<sub>3</sub> on the phase transition behavior, we performed identical tensile strain simulations using  $\beta$  and  $\gamma$ -phase Ga<sub>2</sub>O<sub>3</sub> structures containing 10% Sc or Al. As depicted in Figure 4f, 10% Al alloying results in a slightly lower critical strain and a reduced energy barrier for formation of the γ phase, while 10% Sc alloys exhibit similar trends in overall strain energy density compared to unalloyed Ga<sub>2</sub>O<sub>3</sub>. This observation demonstrates that phase transformation between the  $\beta$  and  $\gamma$  phases can be induced by elongational tensile strain, regardless of alloying with other isovalent oxides. Furthermore, it highlights the potential impact of alloying on the phase transition, especially for Al<sub>2</sub>O<sub>3</sub> alloyed Ga<sub>2</sub>O<sub>3</sub>.

#### CONCLUSIONS

In this study, a thin γ-Ga<sub>2</sub>O<sub>3</sub> layer was identified on top of the surface of bulk grown Sc and Al-alloyed β-Ga<sub>2</sub>O<sub>3</sub> crystals after mechanical exfoliation. The structure and bonding of the  $\gamma$ phase were fully investigated using atomic resolution STEM and EELS indicating a disordered thin film of  $\gamma$  phase (10–20 nm) on the exfoliated surface of the crystal. Electron diffraction confirmed the presence of γ-Ga<sub>2</sub>O<sub>3</sub>, as well as further establishing relationship orientations between the two phases. Using monochromated EELS, the oxygen local environment was probed, and distinct ELNES were identified for the  $\beta$  and  $\gamma$ phases, indicating structural changes to local oxygen coordination between the two regions. Many-body studies conducted on top of DFT provided further insight into the nature of the double peak O K-edge ELNES structure observed in  $\gamma$ -Ga<sub>2</sub>O<sub>3</sub>, revealing the A peak to be excitonic and the B peak to be electronic in nature. To understand the origin of the formation of the γ-Ga<sub>2</sub>O<sub>3</sub> layer over the beta phase, we have performed computational studies and have shown that under certain potential applied conditions, strain can change the energy landscape to induce a transformation from the  $\beta$  to  $\gamma$ phase. This work is vital in providing a potential demonstration for the hypothesis put forward by Huang et al., i.e., that a concentration of defects and strain can lead to γ-Ga<sub>2</sub>O<sub>3</sub> formation. This also marks the first such identification of  $\gamma$ - $Ga_2O_3$  forming on the surface of melt grown  $\beta$ - $Ga_2O_3$ , with prior studies always observing the gamma phase in the form of inclusions and in the context of thin films. Our investigation can help inform thin-film and melt-growth techniques as well as the postprocessing steps before incorporation of Ga<sub>2</sub>O<sub>3</sub> into electronic devices. Understanding the appearance and formation of  $\gamma$ -Ga<sub>2</sub>O<sub>3</sub> in the presence of  $\beta$ -Ga<sub>2</sub>O<sub>3</sub> at the atomic scale is also vital for considering the role that alloying elements and defects may play in this unintentional phase formation. Future studies are needed to understand the exact dynamics and nature of the phase transformation and other conditions that may lead to  $\gamma$ -Ga<sub>2</sub>O<sub>3</sub> formation.

## MATERIALS AND METHODS

Materials Characterization. Bulk  $\beta$ -Ga<sub>2</sub>O<sub>3</sub> crystals were grown from a melt via the Czochralski method described in previous studies. <sup>20,21,56</sup> Pieces were then broken off of the growth boule with a (100) surface orientation via mechanical exfoliation using a razor blade. Select samples were indented with a Leco Vickers microhardness indenter at a load of 1 N in an attempt to characterize the effect of compressive strain on the formation of the  $\gamma$ -phase. Transmission electron microscopy (TEM) lamellae were prepared using a FEI Helios 660 Dual Beam Focused Ion Beam, with initial trenching and milling performed at 30 kV. Further thinning was performed at 5 kV, while final polishing was performed at 2 and 1 kV to reduce the effects of surface damage. Selected area electron diffraction (SAED), bright field (BF)/dark field (DF) TEM, and XEDS was performed on a FEI Talos 200X at an accelerating voltage of 200 kV. Atomic resolution annular dark field (ADF) and annular bright field (ABF) STEM was performed on a double Cs corrected FEI Titan G2 60-300 at an accelerating voltage of 300 kV, with a convergence angle of 21.3 mrad. A detector with a collection angle of 4.6-48.9 mrad was used for ABF-STEM imaging, while a range of 42-244 mrad was used for ADF-STEM imaging. EELS measurements were performed using a double spherical aberration (Cs) corrected FEI Titan G2 60-300 TEM instrument equipped with a monochromator. The scans were performed at an accelerating voltage of 300 kV, with a full-width halfmaximum energy resolution of the zero-loss peak at 0.23 eV. The collection semiangle used for monochromated EELS was 10.1 mrad, and dwell times of 0.5 s and exposure times of 2 s were used during spectral collection.

**Image Simulation.** STEM image simulations were performed using the Prismatic software. The simulated parameters used an accelerating voltage of 300 kV, Cs = 300 nm, and 16 frozen phonons to accommodate all of the thermal configurations. ADF-STEM simulated images were constructed with an annular range of 42–244 mrad, while ABF-STEM simulated images were constructed with a range of 4.5–49 mrad to match experimental collection conditions.

Computational Details. First-principles simulations were carried out using DFT with the projector augmented wave (PAW) method as implemented in the Vienna Ab Initio Simulation Package (VASP). 41,58-62 We utilized the Perdew-Burke-Ernzerhof (PBE) parametrization of the generalized gradient approximation (GGA) to describe the exchange-correlation functional, treating Ga 3d electrons as valence states in all simulations. The plane-wave basis cutoff was set to 420 eV. The atomic geometries of defective spinel structures of the γ-phase were obtained from Ratcliff et al.'s work, <sup>53</sup> in which more than one million structures were screened to obtain low-energy configurations for the  $\gamma$ -phase. The lowest energy structures were individually chosen from both the so-called "3-site" and "4-site" disordered models. Here, the "N-site" models in Ratcliff et al.'s work  $^{46}$ refer to  $\gamma$ -phase structures where Ga atoms are present in N different Wyckoff sites (N = 2, 3, and 4) among the four total Wyckoff sites experimentally identified by Playford et al.<sup>30</sup> Notably, they exhibited enhanced stability of structures and more realistic site occupancy as confirmed by neutron diffraction experiments compared to the traditional 2-site models commonly used for regular spinel structures. The 3 and 4-site  $\gamma$ -phase structures used in this study contained 160 atoms (with supercell dimensions of  $3 \times 1 \times 1$ ) and incorporated long-range disorder of Ga vacancies.

To ensure structural compatibility between the  $\beta$ - and  $\gamma$ -phases, we constructed new  $\beta$  phase supercells that both match the anion framework of the  $\gamma$ -phase structure and exhibit lattice vectors that are nearly commensurate with those of the  $\gamma$ -phase structure. This new  $\beta$  supercell is included in the Supporting Information. Using these  $\beta$ -phase supercells, various effects of mechanical strain were directly compared. To identify the lowest energy structure for  $\beta$ - and  $\gamma$ -phase alloys incorporating 10% Sc or 10% Al, we generated ten different structures for each alloy type. Each structure was created by randomly substituting 6 Ga atoms with Sc or Al atoms, out of a total of 64, from the  $\beta$ -phase and the lowest energy 3-site  $\gamma$ -phase structures. Two different approaches were employed: one maintained an interatomic

distance of 5.85 Å between the substituted alloy atoms, while the other did not impose this constraint (pure random). Although it has been suggested in prior DFT simulations that in the  $\hat{\beta}$  phase, octahedral sites are preferentially occupied by Al<sup>63</sup> and Sc,<sup>64</sup> we did not consider specific occupation preferences in Sc and Al alloy models in either phase. Instead, we selected sites for alloy atoms randomly in both phases. This choice was made because the prior predicted octahedral site preference of Sc/Al in the  $\beta$  phase was based on isolated substitutional values, which may not hold in a 10% alloy beyond conventional dilute limits. Subsequently, we conducted relaxation of all the structures and selected the ones with the lowest energy to represent the  $\beta$ - and  $\gamma$ -phase alloy structures. Although our screening of total 10 structures is admittedly limited in size, we did not observe notable energy differences between the two groups less than 5 meV/atom for all alloy types, suggesting that site preferences and clustering/nonclustering behaviors do not alter our main findings and conclusions. A  $1 \times 3 \times 3$  k-point grid generated by the Monkhorst–Pack method was used. For geometry optimization, we employed a convergence criterion of  $1 \times 10^{-4}$  eV for energy and 0.02 eV/Å for residual forces on each atom. Shear and both uniaxial tensile and compressive strains were applied to this supercell for both phases to compare total energies.

X-ray absorption spectra were derived from the solution of the BSE implemented in the full-potential, all-electron exciting code and applied on top of DFT (PBE functional). A cutoff of  $R_{\rm MT}G_{\rm max}=8.0$  was selected for the plane wave component of the basis set for both structures, and muffin-tin radii of 1.46 (1.6) bohr for oxygen atoms and 1.74 (1.85) bohr for gallium atoms were used for the  $\gamma$  ( $\beta$ ) phase. The BSE was solved on a  $4\times4\times4$  ( $2\times8\times4$ ) k/q-point grid shifted from the  $\Gamma$ -point. To compute the statically screened Coulomb interaction in the random-phase approximation, 100 unoccupied bands were accounted for. Transitions from the oxygen 1s states were included up to an energy range of 30 eV. A scissors operator of 28 eV was applied to reconcile the BSE and IPA results with the experimental data. A Lorentzian broadening of 0.5 eV was employed to visualize the spectra.

## ASSOCIATED CONTENT

# Supporting Information

The Supporting Information is available free of charge at https://pubs.acs.org/doi/10.1021/acsaelm.4c00762.

Additional figures for STEM, EELS, and DFT experiments, including HRTEM, BF-TEM imaging, location of SAED collection, XEDS maps, deconvolution of O K edge, core loss EELS, and density of states calculations (PDF)

Structure file of  $\gamma$ -(Al $_{0.1}$ Ga $_{0.9}$ ) $_2$ O $_3$  supercell (CIF) Structure file of  $\beta$ -(Sc $_{0.1}$ Ga $_{0.9}$ ) $_2$ O $_3$  supercell (CIF) Structure file of  $\gamma$ -(Sc $_{0.1}$ Ga $_{0.9}$ ) $_2$ O $_3$  supercell (CIF) Structure file of  $\beta$ -Ga $_2$ O $_3$  (CIF) Structure file of  $\gamma$ -Ga $_2$ O $_3$  (CIF) Structure file of  $\beta$ -Ga $_2$ O $_3$  supercell (CIF) Structure file of  $\gamma$ -Ga $_2$ O $_3$  3-site supercell (CIF)

Structure file of  $\gamma$ -Ga<sub>2</sub>O<sub>3</sub> 4-site supercell (CIF) Structure file of  $\beta$ -(Al<sub>0.1</sub>Ga<sub>0.9</sub>)<sub>2</sub>O<sub>3</sub> supercell (CIF)

# AUTHOR INFORMATION

## **Corresponding Authors**

Andrew R. Balog — Department of Materials Science and Engineering, Materials Research Institute, The Pennsylvania State University, University Park, Pennsylvania 16802, United States; orcid.org/0009-0002-4133-6849; Email: arb6059@psu.edu

Nasim Alem – Department of Materials Science and Engineering, Materials Research Institute, The Pennsylvania State University, University Park, Pennsylvania 16802, 

#### **Authors**

Channyung Lee — Department of Mechanical Science and Engineering, University of Illinois at Urbana—Champaign, Urbana, Illinois 61801, United States

Daniel Duarte-Ruiz — Institute of Physics, Carl von Ossietzky University Oldenburg, Oldenburg D-26111, Germany; orcid.org/0000-0003-2424-1397

Sai Venkata Gayathri Ayyagari — Department of Materials Science and Engineering, Materials Research Institute, The Pennsylvania State University, University Park, Pennsylvania 16802, United States

Jani Jesenovec — Institute of Materials Research and School of Mechanical and Materials Engineering, Washington State University, Pullman, Washington 99164, United States

Adrian E. Chmielewski — Department of Materials Science and Engineering, Materials Research Institute, The Pennsylvania State University, University Park, Pennsylvania 16802, United States; orcid.org/0000-0003-2373-5061

Leixin Miao – Department of Materials Science and Engineering, Materials Research Institute, The Pennsylvania State University, University Park, Pennsylvania 16802, United States

Benjamin L. Dutton — Institute of Materials Research and School of Mechanical and Materials Engineering, Washington State University, Pullman, Washington 99164, United States

John McCloy — Institute of Materials Research and School of Mechanical and Materials Engineering, Washington State University, Pullman, Washington 99164, United States;
orcid.org/0000-0001-7476-7771

Caterina Cocchi — Institute of Physics, Carl von Ossietzky University Oldenburg, Oldenburg D-26111, Germany; orcid.org/0000-0002-9243-9461

Elif Ertekin — Department of Mechanical Science and Engineering and Materials Research Laboratory, University of Illinois at Urbana—Champaign, Urbana, Illinois 61801, United States; orcid.org/0000-0002-7816-1803

Complete contact information is available at: https://pubs.acs.org/10.1021/acsaelm.4c00762

#### **Author Contributions**

The manuscript was written through contributions of all authors. All authors have given approval to the final version of the manuscript. A.R.B.: writing original draft and editing, data acquisition, and data analysis. C.L.: DFT calculations, data analysis, writing, and editing. D.D.-R.: DFT calculations, data analysis, writing, and editing. S.V.G.A.: STEM image simulations. J.J.: sample fabrication, editing. A.E.C.: data acquisition, data analysis, editing. L.M.: editing. B.L.D.: sample fabrication, editing. J.M.: validation, writing-review, editing. C.C.: validation, writing-review, and editing. N.A.: validation, editing, funding acquisition, project administration, and supervision.

#### Notes

The authors declare no competing financial interest.

## ACKNOWLEDGMENTS

The work at PSU, UIUC, and WSU was supported by the Air Force Office of Scientific Research (AFOSR) program FA9550-21-1-0078 "Fundamentals of Doping and Defects in

β-Ga<sub>2</sub>O<sub>3</sub> for high breakdown fields," Utah-WSU-UIUC-PSU MURI. Work at PSU was also supported by the National Science Foundation through the Pennsylvania State University Materials Research Science and Engineering Center (MRSEC) DMR-2011839 (2020-2026). This work used PSC Bridges-2 at the Pittsburgh Supercomputing Center through allocation MAT220011 from the Advanced Cyberinfrastructure Coordination Ecosystem: Services & Support (ACCESS) program, which is supported by National Science Foundation grants #2138259, #2138286, #2138307, #2137603, and #2138296. D.D.-R. and C.C. acknowledge financial support to the German Ministry for Education and Research (BMBF), Project No. 03XP0328C and Professorinnenprogramm III, and from the State of Lower Saxony (Professorinnen für Niedersachsen). Computational resources were provided by the high-performance computing cluster CARL at the University of Oldenburg, funded by the German Research Foundation (Project No. INST 184/157-1 FUGG) and by the Ministry of Science and Culture of the Lower Saxony State.

#### REFERENCES

- (1) Pearton, S. J.; Yang, J.; Cary, P. H.; Ren, F.; Kim, J.; Tadjer, M. J.; Mastro, M. A. A Review of Ga<sub>2</sub>O<sub>3</sub> Materials, Processing, and Devices. *Appl. Phys. Rev.* **2018**, *5* (1), No. 011301.
- (2) Zhang, J.; Shi, J.; Qi, D. C.; Chen, L.; Zhang, K. H. L. Recent Progress on the Electronic Structure, Defect, and Doping Properties of Ga<sub>2</sub>O<sub>3</sub>. APL Mater. **2020**, 8 (2), No. 020906.
- (3) Green, A. J.; Speck, J.; Xing, G.; Moens, P.; Allerstam, F.; Gumaelius, K.; Neyer, T.; Arias-Purdue, A.; Mehrotra, V.; Kuramata, A.; Sasaki, K.; Watanabe, S.; Koshi, K.; Blevins, J.; Bierwagen, O.; Krishnamoorthy, S.; Leedy, K.; Arehart, A. R.; Neal, A. T.; Mou, S.; Ringel, S. A.; Kumar, A.; Sharma, A.; Ghosh, K.; Singisetti, U.; Li, W.; Chabak, K.; Liddy, K.; Islam, A.; Rajan, S.; Graham, S.; Choi, S.; Cheng, Z.; Higashiwaki, M.  $\beta$ -Gallium Oxide Power Electronics. *APL Mater.* **2022**, *10* (2), No. 029201.
- (4) Higashiwaki, M.; Sasaki, K.; Murakami, H.; Kumagai, Y.; Koukitu, A.; Kuramata, A.; Masui, T.; Yamakoshi, S. Recent Progress in Ga<sub>2</sub>O<sub>3</sub> Power Devices. *Semicond. Sci. Technol.* **2016**, 31 (3), No. 034001.
- (5) Higashiwaki, M.; Sasaki, K.; Kuramata, A.; Masui, T.; Yamakoshi, S. Development of Gallium Oxide Power Devices. *Phys. Status Solidi A* **2014**, 211 (1), 21–26.
- (6) Yoshioka, S.; Climenhaga, V.; Fisher, T.; Thompson, D. J.; Levi, A.; Sasselov, D.; Podolak, M.; Hayashi, H.; Kuwabara, A.; Oba, F.; Matsunaga, K.; Tanaka, I. Structures and Energetics of Ga<sub>2</sub>O<sub>3</sub> Polymorphs. *J. Phys.: Condens. Matter* **2007**, *19* (34), No. 346211.
- (7) Johnson, J. M.; Chen, Z.; Varley, J. B.; Jackson, C. M.; Farzana, E.; Zhang, Z.; Arehart, A. R.; Huang, H. L.; Genc, A.; Ringel, S. A.; Van De Walle, C. G.; Muller, D. A.; Hwang, J. Unusual Formation of Point-Defect Complexes in the Ultrawide-Band-Gap Semiconductor β-Ga<sub>2</sub>O<sub>3</sub>. *Phys. Rev. X* **2019**, 9 (4), No. 041027.
- (8) Ueda, O.; Ikenaga, N.; Koshi, K.; Iizuka, K.; Kuramata, A.; Hanada, K.; Moribayashi, T.; Yamakoshi, S.; Kasu, M. Structural Evaluation of Defects in  $\beta$ -Ga<sub>2</sub>O<sub>3</sub> Single Crystals Grown by Edge-Defined Film-Fed Growth Process. *Jpn. J. Appl. Phys.* **2016**, *55* (12), No. 1202BD.
- (9) Hanada, K.; Moribayashi, T.; Koshi, K.; Sasaki, K.; Kuramata, A.; Ueda, O.; Kasu, M. Origins of Etch Pits in  $\beta$ -Ga<sub>2</sub>O<sub>3</sub> (010) Single Crystals. *Jpn. J. Appl. Phys.* **2016**, 55 (12), 1202BG.
- (10) Fu, B.; Jia, Z.; Mu, W.; Yin, Y.; Zhang, J.; Tao, X. A Review of  $\beta$ -Ga<sub>2</sub>O<sub>3</sub> Single Crystal Defects, Their Effects on Device Performance and Their Formation Mechanism. *J. Semicond.* **2019**, 40 (1), No. 011804.
- (11) Huang, H.-L.; Chae, C.; Hwang, J. Perspective on Atomic Scale Investigation of Point and Extended Defects in Gallium Oxide. *J. Appl. Phys.* **2022**, *131* (19), No. 190901.

- (12) Tadjer, M. J.; Lyons, J. L.; Nepal, N.; Freitas, J. A.; Koehler, A. D.; Foster, G. M. Theory and Characterization of Doping and Defects in  $\beta$ -Ga<sub>2</sub>O<sub>3</sub>. ECS J. Solid State Sci. Technol. **2019**, 8 (7), Q3187—O3194.
- (13) Chmielewski, A.; Deng, Z.; Saleh, M.; Jesenovec, J.; Windl, W.; Lynn, K.; McCloy, J.; Alem, N. Atomic-Scale Characterization of Structural and Electronic Properties of Hf Doped  $\beta$ -Ga<sub>2</sub>O<sub>3</sub>. Appl. Phys. Lett. **2021**, 119 (17), No. 172102.
- (14) Johnson, J. M.; Huang, H. L.; Wang, M.; Mu, S.; Varley, J. B.; Uddin Bhuiyan, A. F. M. A.; Feng, Z.; Kalarickal, N. K.; Rajan, S.; Zhao, H.; Van de Walle, C. G.; Hwang, J. Atomic Scale Investigation of Aluminum Incorporation, Defects, and Phase Stability in  $\beta$ -(Al<sub>x</sub>Ga<sub>1-x</sub>)<sub>2</sub>O<sub>3</sub> Films. *APL Mater.* **2021**, *9* (5), No. 051103.
- (15) Chmielewski, A.; Deng, Z.; Moradifar, P.; Miao, L.; Zhang, Y.; Mauze, A.; Lopez, K. A.; Windl, W.; Alem, N. Spatially Resolved Investigation of the Bandgap Variation across a  $\beta$ -(Al<sub>x</sub>Ga<sub>1-x</sub>)<sub>2</sub>O<sub>3</sub>/ $\beta$ -Ga<sub>2</sub>O<sub>3</sub> Interface by STEM-VEELS. ACS Appl. Electron. Mater. **2022**, 4 (2), 585–591.
- (16) Yoo, T.; Xia, X.; Ren, F.; Jacobs, A.; Tadjer, M. J.; Pearton, S.; Kim, H. Atomic-Scale Characterization of Structural Damage and Recovery in Sn Ion-Implanted  $\beta$ -Ga<sub>2</sub>O<sub>3</sub>. *Appl. Phys. Lett.* **2022**, *121* (7), No. 072111.
- (17) Chmielewski, A. E.; Deng, Z.; Duarte-Ruiz, D.; Moradifar, P.; Miao, L.; Zhang, Y.; Mauze, A.; Cocchi, C.; Windl, W.; Alem, N. Al Coordination and Ga Interstitial Stability in a  $\beta$ -(Al<sub>0.2</sub>Ga<sub>0.8</sub>)<sub>2</sub>O<sub>3</sub> Thin Film. ACS Appl. Mater. Interfaces **2023**, 15 (6), 8601–8608.
- (18) Ranga, P.; Bhattacharyya, A.; Chmielewski, A.; Roy, S.; Sun, R.; Scarpulla, M. A.; Alem, N.; Krishnamoorthy, S. Growth and Characterization of Metalorganic Vapor-Phase Epitaxy-Grown  $\beta$ -(Al<sub>x</sub>Ga<sub>1-x</sub>)<sub>2</sub>O<sub>3</sub>/ $\beta$ -Ga<sub>2</sub>O<sub>3</sub> Heterostructure Channels. *Appl. Phys. Express* **2021**, *14* (2), No. 025501.
- (19) Chang, C. S.; Tanen, N.; Protasenko, V.; Asel, T. J.; Mou, S.; Xing, H. G.; Jena, D.; Muller, D. A.  $\gamma$ -Phase Inclusions as Common Structural Defects in Alloyed  $\beta$ -(Al<sub>x</sub>Ga<sub>1-x</sub>)<sub>2</sub>O<sub>3</sub> and Doped  $\beta$ -Ga<sub>2</sub>O<sub>3</sub> Films. *APL Mater.* **2021**, *9* (5), No. 051119.
- (20) Jesenovec, J.; Dutton, B. L.; Remple, C.; Smith-Gray, N.; Murugesan, M.; Peterson, C.; Downing, B. K.; Krishnamoorthy, S.; McCluskey, M. D.; McCloy, J. S. Alternative Alloy to Increase Bandgap in Gallium Oxide,  $\beta$ -(Sc<sub>x</sub>Ga<sub>1-x</sub>)<sub>2</sub>O<sub>3</sub>, and Rare Earth Stark Luminescence. *J. Cryst. Growth* **2022**, 596, No. 126823.
- (21) Jesenovec, J.; Dutton, B.; Stone-Weiss, N.; Chmielewski, A.; Saleh, M.; Peterson, C.; Alem, N.; Krishnamoorthy, S.; McCloy, J. S. Alloyed  $\beta$ -(Al $_x$ Ga $_{1-x}$ ) $_2$ O $_3$  Bulk Czochralski Single  $\beta$ -(Al $_0$ 1Ga $_0$ 9) $_2$ O $_3$  and Polycrystals  $\beta$ -(Al $_0$ 13Ga $_0$ 66) $_2$ O $_3$ 9,  $\beta$ -(Al $_0$ 5Ga $_0$ 5) $_2$ O $_3$ 9, and Property Trends. *J. Appl. Phys.* **2022**, *131* (15), No. 155702.
- (22) Wang, T.; Li, W.; Ni, C.; Janotti, A. Band Gap and Band Offset of  $Ga_2O_3$  and  $(Al_xGa_{1-x})_2O_3$  Alloys. *Phys. Rev. Appl.* **2018**, 10 (1), No. 011003.
- (23) Knop, O.; Hartley, J. M. Refinement of the Crystal Structure of Scandium Oxide. *Can. J. Chem.* **1968**, *46* (8), 1446–1450.
- (24) Huang, H.-L.; Chae, C.; Johnson, J. M.; Senckowski, A.; Sharma, S.; Singisetti, U.; Wong, M. H.; Hwang, J. Atomic Scale Defect Formation and Phase Transformation in Si Implanted  $\beta$ -Ga<sub>2</sub>O<sub>3</sub>. APL Mater. **2023**, 11 (6), No. 061113.
- (25) Huang, H.-L.; Johnson, J. M.; Chae, C.; Senckowski, A.; Wong, M. H.; Hwang, J. Atomic Scale Mechanism of  $\beta$  to  $\gamma$  Phase Transformation in Gallium Oxide. *Appl. Phys. Lett.* **2023**, 122 (25), No. 251602.
- (26) James, E. M.; Browning, N. D. Practical Aspects of Atomic Resolution Imaging and Analysis in STEM. *Ultramicroscopy* **1999**, 78, 125–139.
- (27) Hÿtch, M. J.; Snoeck, E.; Kilaas, R. Quantitative Measurement of Displacement and Strain Fields from HREM Micrographs. *Ultramicroscopy* **1998**, *74* (3), 131–146.
- (28) Åhman, J.; Svensson, G.; Albertsson, J. A Reinvestigation of  $\beta$ -Gallium Oxide. *Acta Crystallogr. C* **1996**, 52 (6), 1336–1338.
- (29) Geller, S. Crystal Structure of  $\beta$ -Ga<sub>2</sub>O<sub>3</sub>. *J. Chem. Phys.* **1960**, 33, 676–684.

- (30) Galazka, Z. Growth of Bulk  $\beta$ -Ga<sub>2</sub>O<sub>3</sub> Single Crystals by the Czochralski Method. *J. Appl. Phys.* **2022**, 131 (3), No. 031103.
- (31) Playford, H. Y.; Hannon, A. C.; Tucker, M. G.; Dawson, D. M.; Ashbrook, S. E.; Kastiban, R. J.; Sloan, J.; Walton, R. I. Characterization of Structural Disorder in  $\gamma$ -Ga<sub>2</sub>O<sub>3</sub>. *J. Phys. Chem. C* **2014**, *118* (29), 16188–16198.
- (32) García-Fernández, J.; Kjeldby, S. B.; Nguyen, P. D.; Karlsen, O. B.; Vines, L.; Prytz, Ø. Formation of  $\gamma$ -Ga<sub>2</sub>O<sub>3</sub> by Ion Implantation: Polymorphic Phase Transformation of  $\beta$ -Ga<sub>2</sub>O<sub>3</sub>. *Appl. Phys. Lett.* **2022**, *121* (19), No. 191601.
- (33) Okunishi, E.; Sawada, H.; Kondo, Y. Experimental Study of Annular Bright Field (ABF) Imaging Using Aberration-Corrected Scanning Transmission Electron Microscopy (STEM). *Micron* **2012**, 43 (4), 538–544.
- (34) Cocchi, C.; Zschiesche, H.; Nabok, D.; Mogilatenko, A.; Albrecht, M.; Galazka, Z.; Kirmse, H.; Draxl, C.; Koch, C. T. Atomic Signatures of Local Environment from Core-Level Spectroscopy in  $\beta$ -Ga<sub>2</sub>O<sub>3</sub>. *Phys. Rev. B* **2016**, *94* (7), No. 075147.
- (35) Anber, E. A.; Foley, D.; Lang, A. C.; Nathaniel, J.; Hart, J. L.; Tadjer, M. J.; Hobart, K. D.; Pearton, S.; Taheri, M. L. Structural Transition and Recovery of Ge Implanted  $\beta$ -Ga<sub>2</sub>O<sub>3</sub>. *Appl. Phys. Lett.* **2020**, *117* (15), No. 152101.
- (36) Azarov, A.; Bazioti, C.; Venkatachalapathy, V.; Vajeeston, P.; Monakhov, E.; Kuznetsov, A. Disorder-Induced Ordering in Gallium Oxide Polymorphs. *Phys. Rev. Lett.* **2022**, *128*, No. 015704.
- (37) Azarov, A.; Fernández, J. G.; Zhao, J.; Djurabekova, F.; He, H.; He, R.; Prytz, Ø.; Vines, L.; Bektas, U.; Chekhonin, P.; Klingner, N.; Hlawacek, G.; Kuznetsov, A. Universal Radiation Tolerant Semiconductor. *Nat. Commun.* **2023**, *14* (1), 4855.
- (38) Sharma, A.; Varshney, M.; Shin, H. J.; Chae, K. H.; Won, S. O. Investigation on Cation Distribution and Luminescence in Spinel Phase  $\gamma$ -Ga<sub>3- $\delta$ </sub>O<sub>4</sub>: Sm Nanostructures Using X-Ray Absorption Spectroscopy. *RSC Adv.* **2017**, 7 (83), 52543–52554.
- (39) Chen, J. G. NEXAFS Investigations of Transition Metal Oxides, Nitrides, Carbides, Sulfides and Other Interstitial Compounds. *Surf. Sci. Rep.* **1997**, *30* (1), 1–152.
- (40) Swallow, J. E. N.; Vorwerk, C.; Mazzolini, P.; Vogt, P.; Bierwagen, O.; Karg, A.; Eickhoff, M.; Schörmann, J.; Wagner, M. R.; Roberts, J. W.; Chalker, P. R.; Smiles, M. J.; Murgatroyd, P.; Razek, S. A.; Lebens-Higgins, Z. W.; Piper, L. F. J.; Jones, L. A. H.; Thakur, P. K.; Lee, T. L.; Varley, J. B.; Furthmüller, J.; Draxl, C.; Veal, T. D.; Regoutz, A. Influence of Polymorphism on the Electronic Structure of Ga<sub>2</sub>O<sub>3</sub>. *Chem. Mater.* **2020**, 32 (19), 8460–8470.
- (41) Kohn, W.; Sham, L. J. Self-Consistent Equations Including Exchange and Correlation Effects. *Phys. Rev.* **1965**, *140* (4A), A1133–A1138.
- (42) Gulans, A.; Kontur, S.; Meisenbichler, C.; Nabok, D.; Pavone, P.; Rigamonti, S.; Sagmeister, S.; Werner, U.; Draxl, C. Exciting: A Full-Potential All-Electron Package Implementing Density-Functional Theory and Many-Body Perturbation Theory. *J. Phys.: Condens. Matter* 2014, 26 (36), No. 363202.
- (43) Onida, G.; Reining, L.; Rubio, A. Electronic Excitations: Density-Functional versus Many-Body Green's-Function Approaches. *Rev. Mod. Phys.* **2002**, *74* (2), 601–659.
- (44) Vorwerk, C.; Aurich, B.; Cocchi, C.; Draxl, C. Bethe—Salpeter Equation for Absorption and Scattering Spectroscopy: Implementation in the Exciting Code. *Electron. Struct.* **2019**, *1* (3), No. 037001.
- (45) Ferreira, Machado; de Araujo, F.; Duarte-Ruiz, D.; Saßnick, H.-D.; Gentzmann, M. C.; Huthwelker, T.; Cocchi, C. Electronic Structure and Core Spectroscopy of Scandium Fluoride Polymorphs. *Inorg. Chem.* **2023**, *62* (10), 4238–4247.
- (46) Lion, K.; Cocchi, C.; Draxl, C. X-Ray Absorption Spectroscopy of Oligothiophene Crystals from Many-Body Perturbation Theory. *Phys. Rev. Mater.* **2024**, *8* (2), No. 024603.
- (47) Ruiz, D. D.; Cocchi, C. First-Principles Core Spectroscopy of LiCoO<sub>2</sub> and CoO<sub>2</sub>. *J. Phys. Chem. C* **2022**, 126 (27), 10949–10956. (48) Cocchi, C. X-Ray Absorption Fingerprints from Cs Atoms in Cs<sub>3</sub>Sb. *Phys. Status Solidi RRL–Rapid Res. Lett.* **2020**, 14 (7), No. 2000194.

- (49) Cocchi, C.; Draxl, C. Bound Excitons and Many-Body Effects in x-Ray Absorption Spectra of Azobenzene-Functionalized Self-Assembled Monolayers. *Phys. Rev. B* **2015**, 92 (20), No. 205105.
- (50) Cocchi, C.; Draxl, C. Optical Spectra from Molecules to Crystals: Insight from Many-Body Perturbation Theory. *Phys. Rev. B* **2015**, 92 (20), No. 205126.
- (51) Wu, S.-Q.; Cheng, S.; Lu, L.; Liu, M.; Jin, X.-W.; Cheng, S.-D.; Mi, S.-B. B-Site Ordering and Strain-Induced Phase Transition in Double-Perovskite La<sub>2</sub>NiMnO<sub>6</sub> Films. *Sci. Rep.* **2018**, 8 (1), 2516.
- (52) Xu, Y.; Park, J.-H.; Yao, Z.; Wolverton, C.; Razeghi, M.; Wu, J.; Dravid, V. P. Strain-Induced Metastable Phase Stabilization in Ga<sub>2</sub>O<sub>3</sub> Thin Films. *ACS Appl. Mater. Interfaces* **2019**, *11* (5), 5536–5543.
- (53) Ratcliff, L. E.; Oshima, T.; Nippert, F.; Janzen, B. M.; Kluth, E.; Goldhahn, R.; Feneberg, M.; Mazzolini, P.; Bierwagen, O.; Wouters, C.; Nofal, M.; Albrecht, M.; Swallow, J. E. N.; Jones, L. A. H.; Thakur, P. K.; Lee, T.-L.; Kalha, C.; Schlueter, C.; Veal, T. D.; Varley, J. B.; Wagner, M. R.; Regoutz, A. Tackling Disorder in  $\gamma$ -Ga<sub>2</sub>O<sub>3</sub>. *Adv. Mater.* **2022**, *34* (37), 2204217.
- (54) Sun, R.; Balog, A. R.; Yang, H.; Alem, N.; Scarpulla, M. A. Degradation of  $\beta$ -Ga<sub>2</sub>O<sub>3</sub> Vertical Ni/Au Schottky Diodes Under Forward Bias. *IEEE Electron Device Lett.* **2023**, 44 (5), 725–728.
- (55) Bhuiyan, A. F. M. A. U.; Feng, Z.; Johnson, J. M.; Huang, H. L.; Sarker, J.; Zhu, M.; Karim, M. R.; Mazumder, B.; Hwang, J.; Zhao, H. Phase Transformation in MOCVD Growth of (Al<sub>x</sub>Ga<sub>1-x</sub>)<sub>2</sub>O<sub>3</sub> Thin Films. *APL Mater.* **2020**, *8* (3), No. 031104.
- (56) McCloy, J.; Jesenovec, J.; Dutton, B.; Pansegrau, C.; Remple, C.; Weber, M. H.; Swain, S.; McCluskey, M.; Scarpulla, M.; Growth and Defect Characterization of Doped and Undoped  $\beta$ -Ga<sub>2</sub>O<sub>3</sub> Crystals. In Oxide-based Materials and Devices XIII, 2022; Vol 12002, pp 21–39.
- (57) Rangel DaCosta, L.; Brown, H. G.; Pelz, P. M.; Rakowski, A.; Barber, N.; O'Donovan, P.; McBean, P.; Jones, L.; Ciston, J.; Scott, M. C.; Ophus, C. Prismatic 2.0—Simulation Software for Scanning and High Resolution Transmission Electron Microscopy (STEM and HRTEM). *Micron* 2021, 151, No. 103141.
- (58) Hohenberg, P.; Kohn, W. Inhomogeneous Electron Gas. *Phys. Rev.* **1964**, *136* (3B), B864–B871.
- (59) Blöchl, P. E. Projector Augmented-Wave Method. *Phys. Rev. B* **1994**, *50* (24), 17953–17979.
- (60) Kresse, G.; Joubert, D. From Ultrasoft Pseudopotentials to the Projector Augmented-Wave Method. *Phys. Rev. B* **1999**, *59* (3), 1758–1775.
- (61) Kresse, G.; Furthmüller, J. Efficiency of Ab-Initio Total Energy Calculations for Metals and Semiconductors Using a Plane-Wave Basis Set. *Comput. Mater. Sci.* **1996**, *6* (1), 15–50.
- (62) Kresse, G.; Furthmüller, J. Efficient Iterative Schemes for *Ab Initio* Total-Energy Calculations Using a Plane-Wave Basis Set. *Phys. Rev. B* **1996**, *54* (16), 11169–11186.
- (63) Ma, X.; Zhang, Y.; Dong, L.; Jia, R. First-Principles Calculations of Electronic and Optical Properties of Aluminum-Doped  $\beta$ -Ga<sub>2</sub>O<sub>3</sub> with Intrinsic Defects. *Results Phys.* **2017**, *7*, 1582–1589.
- (64) Zhu, N.; Wang, B.; Ma, K.; Xue, X.; Su, J. Structural Characters and Band Offset of Ga<sub>2</sub>O<sub>3</sub>-Sc<sub>2</sub>O<sub>3</sub> Alloys. *Appl. Phys. Lett.* **2022**, 120 (5), No. 053503.
- (65) Monkhorst, H. J.; Pack, J. D. Special Points for Brillouin-Zone Integrations. *Phys. Rev. B* **1976**, *13* (12), 5188–5192.